Numerical Simulation of Foil Acceleration Experiments with Light Ion Beams

O. Yu. Vorobjev, A. L. Ni, B. Goel
Institut für Neutronenphysik und Reaktortechnik

Kernforschungszentrum Karlsruhe

KERNFORSCHUNGSZENTRUM KARLSRUHE
Institut für Neutronenphysik und Reaktortechnik

KfK 5299

Numerical Simulation of Foil Acceleration Experiments with Light Ion Beams

O. Yu. Vorobjev[1], A. L. Ni[1], B. Goel

[1]) Permanent address;
Institute of Chemical Physics, Chernogolovka, Russia

Abstract

Numerical investigation of the dynamics of foil acceleration experiments performed recently at KALIF is presented. These numerical simulations include realistic physical parameters, e.g., realistic beam power history, wide-range equations of state, effects of the range shortening in hot plasma, electron and radiative heat conduction, etc. Calculations have been performed for the measured beam parameters. Calculated results are compared with experimental measurements of the free surface velocity. Simulations have shown that the beam power density required to successfully reproduce these results for a large number of experiments had to be reduced considerably in amplitude and duration. Some calculations are also presented for light-ion beam parameters that may become available in the near future at KfK.

Numerische Simulation von Folien Beschleunigungsexperimente mit Leicht Ionen Strahlen

Im vorliegenden Bericht sind numerische Simulationen von am KALIF durchgeführten Folien Beschleunigungsexperimenten dargestellt. Die Simulationsrechnungen enthalten realistische physikalische Parametern wie Leistungsverlauf, Zustandsdaten, Reichweiten-Verkürzung in heißem Plasma, Elektron- und Strahlungswärmeleitung usw. Die Rechnungen wurden mit den gemessenen Strahlparametern durchgefürht. Die Rechenergebnisse werden mit den gemessenen Oberflächen- Geschwindigkeiten verglichen. Es ergab sich, daß der zeitliche Verlauf der Strahlprofile sowohl in seiner Höhe als auch in seiner Dauer reduziert werden mußte, um ausreichende Übereinstimmung der Rechenergebnisse mit den Messungen zu erzielen. Zusätzlich wurden einige Rechnungen durchgefürt führ Strahlparameter, die zukünftig im KfK erzielt werden.

1. Introduction

Intense ion beams can be used to generate ultrahigh pressures in condensed matter [1][2]. Light-ion beams generated at the **Karlsruhe Light Ion Facility** (KALIF) typically have a focus of less than 1 cm diameter. The maximum power density achieved to date is of the order of 1 terrawatt per sq.cm. [3]. At the Sandia National Laboratory, power densities up to 5.4 TW/sq.cm. have been reported [4]. These power densities allow pressures in the Mbar regime to be created by the direct interaction of ion beams impinging on the solid targets. This regime can be extended by the use of cumulative systems, such as mutilayered or conical targets. In the energy deposition zone of the targets, the 1.5 MeV protons of the KALIF beam deposit energy of the order of 100 TW/g or 5 MJ/g. A strongly coupled, hot, dense plasma is thus created by the action of a light ion beam on matter. This region of hot dense plasma is of interest also in astrophysical problems. The size of the light ion beam focus is large; as a consequence, two-dimensional effects do not complicate the analysis. KALIF beams allow experiments to be performed in the region of a strongly coupled plasma, a region whose description requires sophisticated theoretical tools. A successful interpretation of beam-target interaction experiments, in the long run, can serve as a check of theoretical models and of the equation of state data based on these models. Also experiments with high-power lasers can produce ultrahigh pressures. In fact, pressures much higher than those that can at present be achieved with light ion beams have been observed in laser experiments. Light-ion beams, however, have the advantage that, due to the large focus size, planar shocks are generated. The absence of hot electrons in light-ion experiments permits shock to propagate in cold materials. The classical mechanism of ion energy deposition

makes the analysis of experiments less ambiguous. Intense ion beams generated with pulsed power machines, such as KALIF, show a change in the beam particle energy and in the focused power density on the target as a function of time. Parts of the target receiving energy from the beam change with the change in the energy of impinging ions. These changes are intensified by the change in target properties (i.e. temperature and density) under intense beam action. A sound numerical scheme is needed to analyze these experiments. This present paper contains an investigation of the dynamics of thin-foil acceleration by light-ion beams and an analyses of various experiments performed recently [5]. The presented numerical calculations include realistic physical parameters, e.g., realistic beam power profiles, wide-range equations of state, effects of the range shortening in hot plasma, electron and radiative heat transfer, etc. Calculations have been performed for the measured beam parameters of KALIF. Some calculations are also presented for light-ion beam parameters that may become available in the near future at KALIF. Calculated results for aluminum foil acceleration by the KALIF beam have been compared with experimental measurements obtained by high-resolution interferometric methods [1]. Simulations have shown that the beam power density required to successfully reproduce these results for a large number of experiments had to be modified in amplitude and duration.

2. Mathematical Model

The Euler equations of motion are used to describe the dynamics of matter under the impact of a beam. They express conservation laws for mass, momentum, and energy.

$$\frac{\partial \rho}{\partial t} + \frac{\partial \rho u}{\partial x} = 0 \tag{2.1}$$

$$\frac{\partial \rho u}{\partial t} + \frac{\partial (\rho u^2 + p)}{\partial x} = 0 \tag{2.2}$$

$$\frac{\partial}{\partial t}[\rho(e + \frac{u^2}{2})] + \frac{\partial}{\partial x}[\rho u(e + \frac{u^2}{2}) + pu - \lambda_e \frac{\partial T}{\partial x} + S_r] = Q(x, t) \tag{2.3}$$

where ρ is the density; p, the pressure; T, the temperature; u, the mass velocity; e, the specific internal energy; and Q(x,t) is the power density deposited in the target by the beam. To describe the dynamic damage of the material we use a continuum-kinetic model obtained on the basis of experimental observation of the velocity profiles of the free surface as the compression pulse reaches the surface and causes a release wave in the target [6]. This model has been used sucessfully to describe ultrahigh strain rates (10^7 s^{-1}) by computer simulation of laser-induced shock loading of a target, and has been found to be in good agreement with the experiment. Equations of porous growth according to the continuum-kinetic model can be written in the conservative form.

$$\frac{\partial \rho V_p}{\partial t} + \frac{\partial \rho u V_p}{\partial x} = \rho \psi(V_p, p) \tag{2.4}$$

where $\psi = dV_p/dt$ is the kinetic function for the porous growth [6] and V_p is the specific porous volume. The caloric equation of state (2.5) is used to close the equations of motion of the (2.1-2.4) system:

$$p = p(e, \rho^{\times}) \quad , \quad \rho^{\times} = \frac{\rho}{1 - \rho V_p} \tag{2.5}$$

The radiative energy transfer is treated in the radiation heat conduction approximation [7]. In this case, the energy flow is proportional to the temperature gradient, the proportionality coefficient being expressed by the Rosseland mean free path, ℓ

$$S_r = -\frac{16\sigma T^3}{3} \ell \frac{\partial T}{\partial x} \tag{2.6}$$

where σ is the Stefan-Boltzmann constant. Thus the conductive energy flow consists of two terms: electron conductivity and radiation conductivity. The electron conductivity coefficient, λ_e, and the Rosseland mean free path, ℓ, are functions of density and temperature and were determined by wide-range semi-empirical formulas developed in [9]. The maximum target temperature reached in present KALIF experiments does not exceed a few 10's of eV. Therefore, the energy of the radiation field is not very important in the calculations reported here and the simple approximation of radiation heat conduction is deemed to be adequate to calculate the radiative heat transfer.

2.1 Equations of State

For the numerical simulation of foil acceleration by the ion beam it is necessary to use an equation of state (EOS) describing, with reasonable accuracy, the shock compression of matter and the plasma thermodynamics in the energy deposition region. In the following calculations, a semi-empirical EOS is used which describes the experimental data on shock compression of the solid samples in the pressure range up to several Mbar. Following the usual procedure, the internal

energy of matter is divided into two parts: The cold energy, E_C, is only a function of density of matter, while the energy of thermal motion, E_T, is a function both of temperature and density.

$$E(p,V) \;=\; E_C(V) \;+\; E_T(p,V) \tag{2.7}$$

The cold component of the energy for solids is represented as a series expansion in the reciprocal interatomic distance, $r^{-1} \sim \sigma^{1/3}$ ($\sigma = V_0/V$, V_0 being the specific volume at $p = 0$, $T = 0$).

$$E_C(V) \;=\; 3V_0 \sum_{i=1}^{5} \frac{a_i}{i} (\sigma^{i/3} - 1) \;, \qquad \sigma > 1 \tag{2.8}$$

Two of the five coefficients in (2.8) are determined by satisfying the following normal conditions

$$P_C(V) \;=\; \left. \frac{dE_C}{dV} \right]_{V = V_0} \;=\; 0 \tag{2.9}$$

$$-V \left. \frac{P_C(V)}{dV} \right]_{V = V_0} \;=\; B_0 \tag{2.10}$$

where B_0 is the bulk modulus of elasticity at ambient condition. The other three coefficients are fitted to describe experimental Hugoniot data. In the expansion region a two-term polynomial is used,

$$E_C(V) \;=\; \frac{B_0 V_0}{m-n} \left[\frac{\sigma^m}{m} - \frac{\sigma^n}{n} \right] + E_{Sub} \qquad \sigma < 1 \tag{2.11}$$

which satisfies the normal condition (2.9-2.10) if

$$n = \frac{B_0 V_0}{m E_{Sub}} \tag{2.12}$$

E_{Sub} is the sublimation energy. The Thermal pressure is related to the thermal energy through the Grüneisen parameter γ, which is represented as a function of energy and density.

$$P_T = \gamma(E,V) \frac{E_T}{V} \tag{2.13}$$

In the presented calculations, two different dependences of γ are used. One (2.14) is as proposed in [10] while the other dependence given in (2.15) is derived to obtain a better fit to the results of quantum-statistical calculations in the region of the dense non-ideal plasma.

$$\gamma(E,V) = \gamma_a - \frac{(\gamma_a - \gamma_C(V))}{1 + (\frac{V}{V_0})^{2/3}(\frac{E - E_C}{E_a})} \tag{2.14}$$

or

$$\gamma = \gamma_a + (\gamma_1(V) - \gamma_a)(1 - (E - E_c)/E_{a'}) \quad , \quad E_t < E_{a'}$$

$$\gamma = \gamma_a + \beta(1 - E_t/E_{a'}) \quad , \quad E_t \geq E_{a'} \tag{2.15}$$

$$\gamma_1 = \gamma_0 + (2/3 - \gamma_0)(1 - (V_0/V)^\alpha) \quad , \quad V \geq V_0$$

$$\gamma_1 = \gamma_0 \quad , \quad V < V_0$$

In (2.15), β, α, $E_{a'}$, and γ_a are fitting parameters. Grüneisen parameter calculations with formulas (2.15) for different energies and densities are plotted together with calculations obtained by quantum-statistical and quantum-mechanical models

[11]. We call the equation of state with the thermal term in the form (2.14) EOS1, and that with γ in form (2.15), EOS2.

The analytical form of EOS is convenient for numerical calculations. It saves simulation time and assures the continuity of pressure and sound velocity over the entire range of simulation. The temperature is calculated by using the tabulated SESAME EOS. The values of pressure and sound velocity for aluminum calculated with the analytical equation of state described above are compared with those of the SESAME table in Fig. 3 and 4. In Fig. 5, the shock Hugoniot adiabats due to the analytical EOS and to the SESAME tables are compared for some metals of interest.
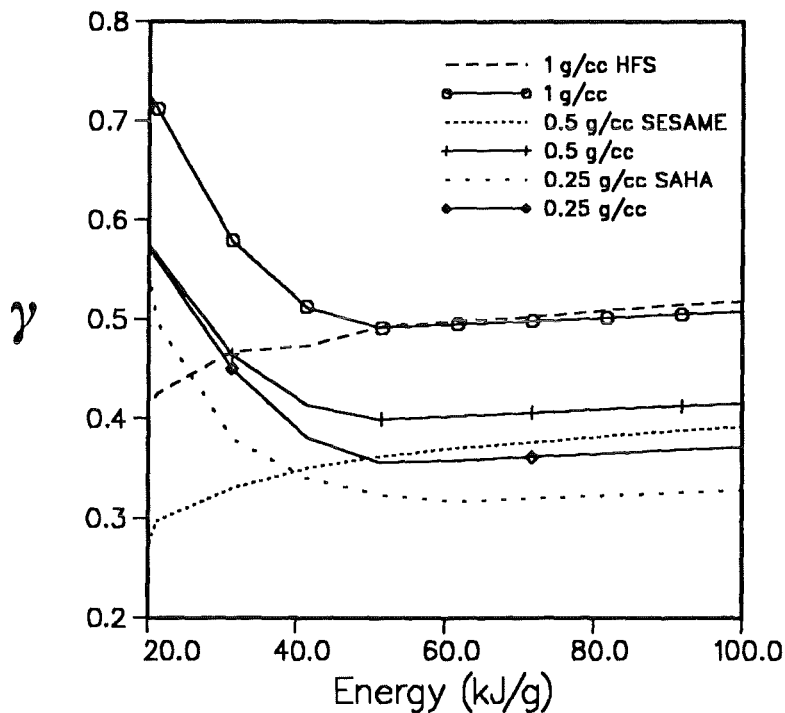
Figure 1. Grüneisen coefficient: The Grüneisen coefficient as a function of the specific internal energy at moderate densities. The solid lines are the results obtained with formula (2.15) for y (EOS2), the dashed lines are the results of theoretical models as metioned in the text. These were converted in the form of Eq. 2.7 for comparison and for use in the calculations.
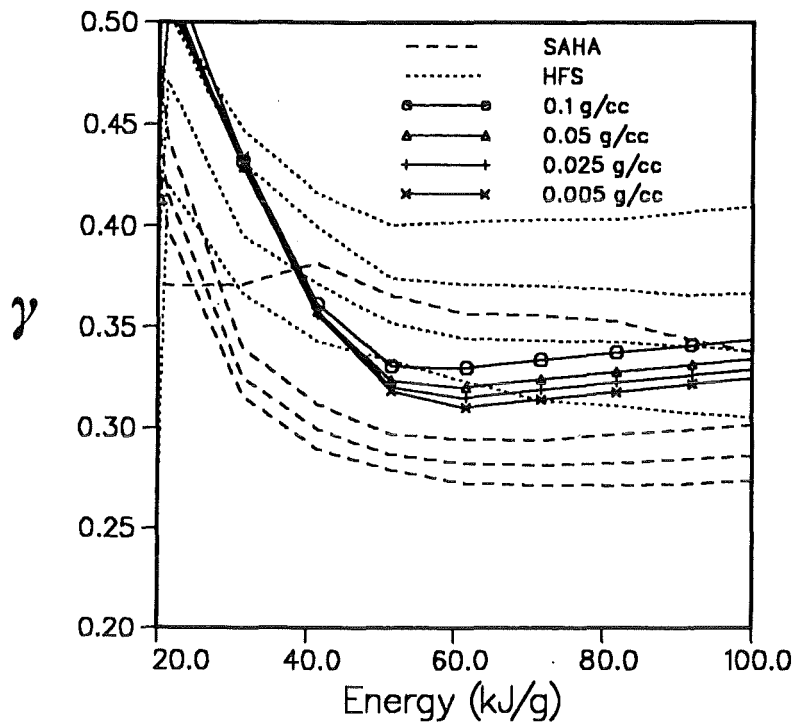
Figure 2. **Grüneisen coefficient:** The Grüneisen coefficient as a function of the specific internal energy at gaseous densities: $\rho = 0.1, 0.05, 0.025, 0.005\,g/cm^3$. The solid lines are EOS2 results obtained with formula (2.15) for γ, the dashed lines are results of other models.
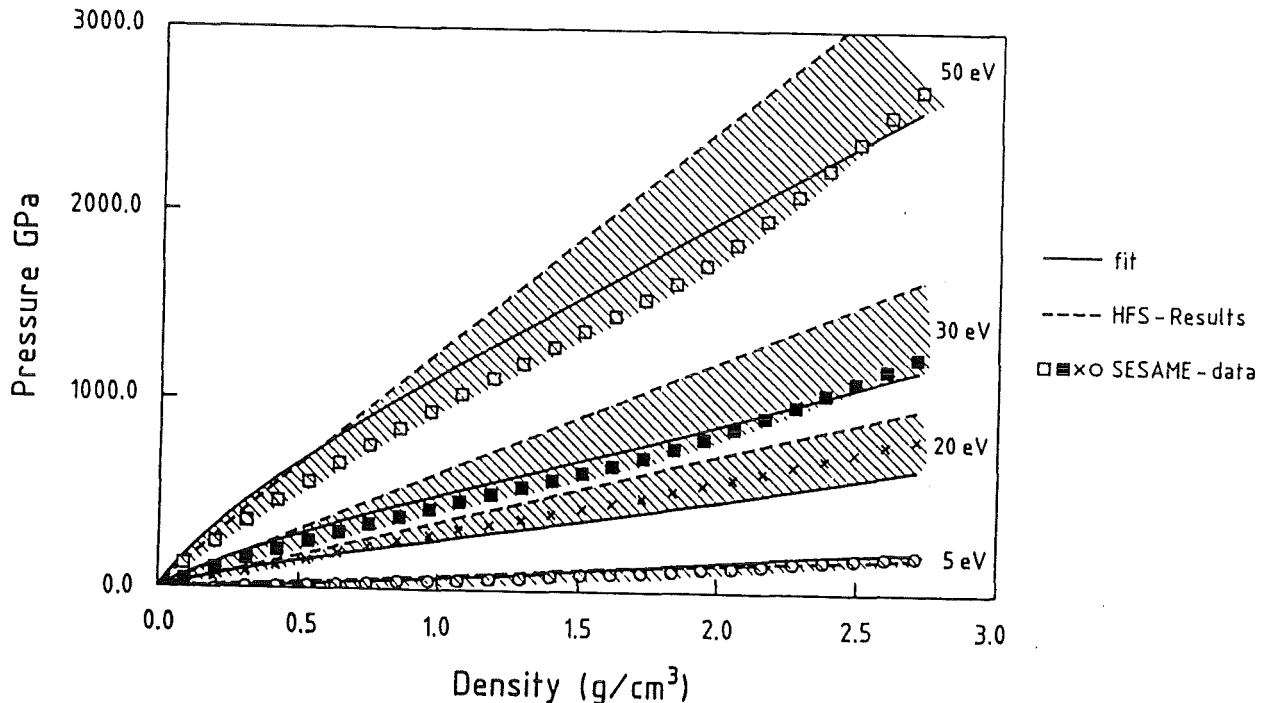
Figure 3. **Pressure:** Pressures calculated for aluminum with the used analytical EOS are compared with those of SESAME EOS data and with the results of Hartree-Fock-Slater calculations of Ref. [11].
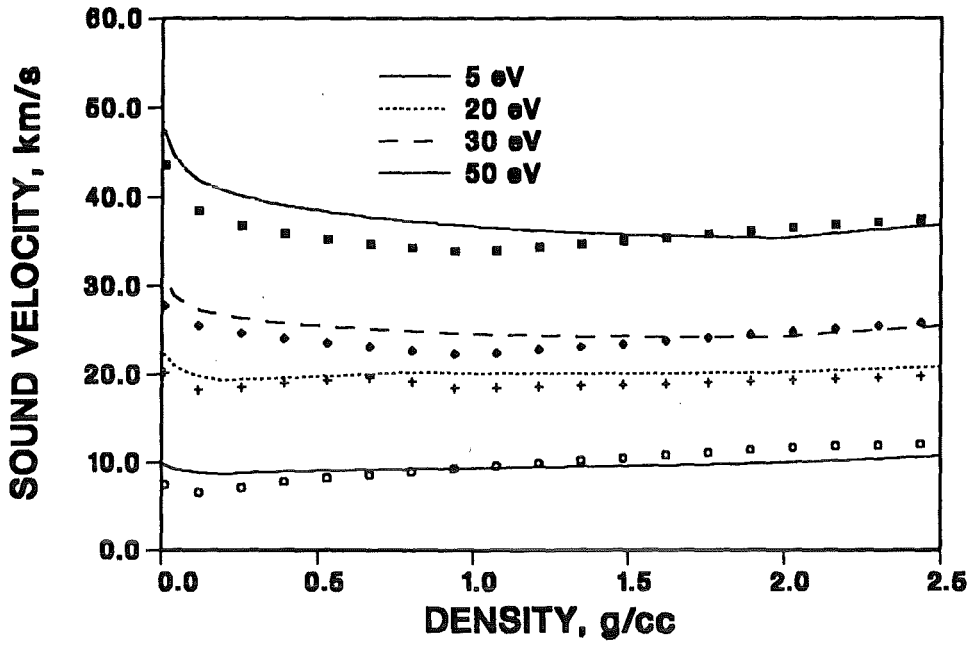
Figure 4. Sound Velocity: Sound velocities calculated for aluminum with the used analytical EOS are compared with those of SESAME data.
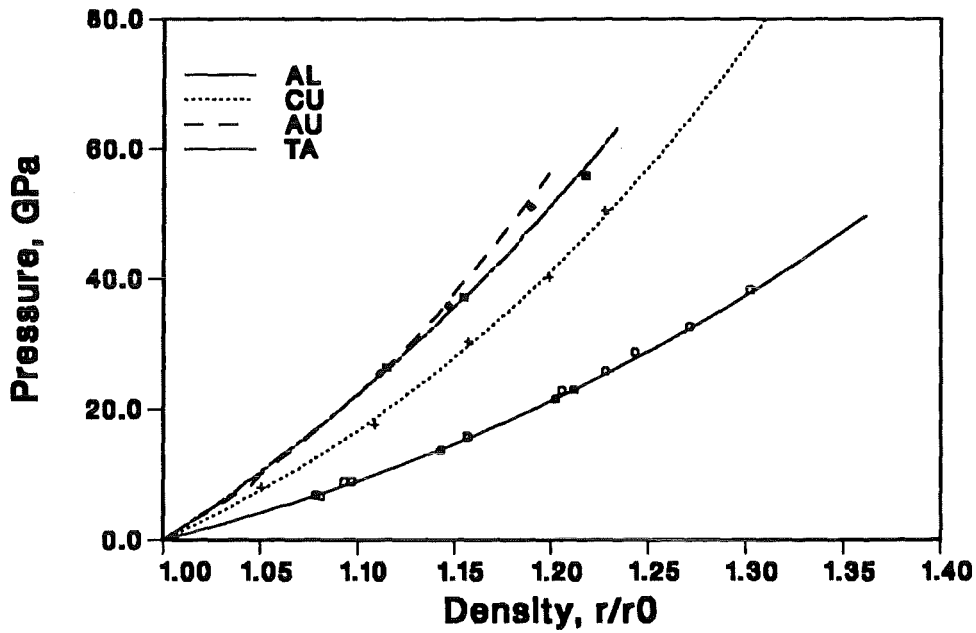
Figure 5. Shock Hugoniot: Schock Hugoniot adiabates for various metals are compared with experimental data. The symbols indicate experimental data, lines are Hugoniots calculated with analytical EOS.

2.2 Energy Deposition Calculation

The absorption of the beam energy by the target is calculated in a single-particle approximation.

$$S = -\frac{1}{\rho}\frac{dE}{dX} = S_\beta + S_{fe} + S_i + S_{nuc} \qquad (2.16)$$

This is based on the assumption that the total stopping power, S, can be represented as the sum of terms describing the contributions by the bound and the free electrons, ions, and nuclei. For these calculations, the stopping power was calculated by the semi-empirical formulas developed in [12][14]. These formulas describe the enhancement of the stopping power as a fuction of heating and the expansion of matter. Results of calculations for 1.5 MeV protons are shown in Fig.6 in comparison with calculations by the model used previously [13]. The main difference between the two models lies in the region of partially ionized plasma. It is a result of the way in which the mean degree of ionization and the mean ionization potential are calculated. The degree of ionization calculated with the two models is compared in Table 1. The difference is in the region of main interest of the present investigations. In a separate calculations, the effect of this discrepancy was assessed and verified not to affect the basic conclusions drawn in this paper.

S (MeV*cm**2/g)

1000.0

800.0

600.0

400.0

200.0

0.0

□————□ Solid
⊖————⊖ 20 eV ρ/100
△————△ 50 eV ρ/100

0.000 0.002 0.004 0.006 0.008 0.010

Range (g*cm**2/g)
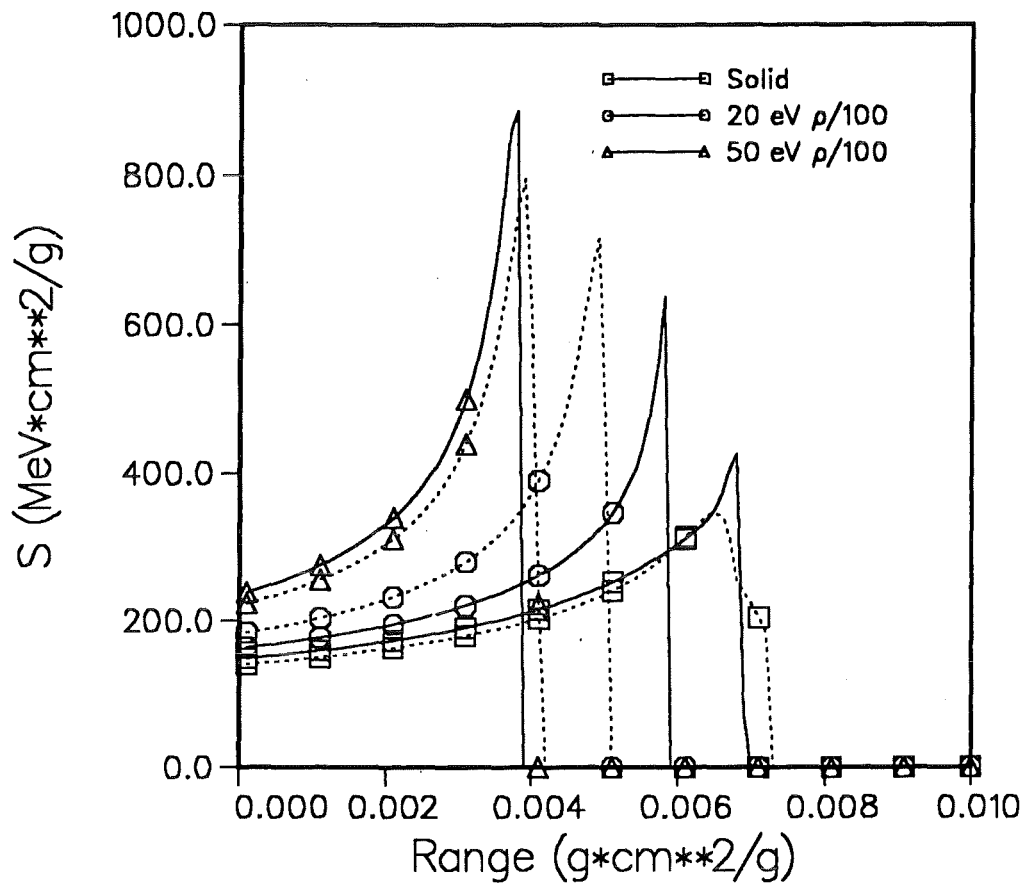
Figure 6. **Stopping power:** Range of 1.5 MeV protons in aluminum in the solid and plasma states. The continuous lines indicate the results of the present model, dashed line, the results of [13].

TABLE 1

The mean degree of ionization used to calculate stopping power

Temperature	Density	$<Z>$ Ref.[14]	Ref. [13]
20 eV	$\rho_s/10$	3.14	3.69
	$\rho_s/100$	3.92	4.58
50 eV	$\rho_s/10$	7.63	6.25
	$\rho_s/100$	9.61	7.53

11

2.3 Numerical Procedure and some Test Calculations

The calculations were performed using the Godunov method with a moving-grid algorithm [15]. The nodes of the grid are moved with contact velocities calculated by solving the Riemann problems between the neighboring cells. The numerical procedure employed allows the Riemann problem to be solved for any equation of state. For the present problem, it is very important to simulate accurately the expansion of the dense plasma heated by the ion beam. To test the code we performed calculations of unloading into vacuum an instantaneously heated aluminum semiplane. The pressure in the heated matter was assumed to be 100 kbar. This is a typical thermal pressure that can be generated in the target during the interaction of the KALIF beam with the target. In Fig. 7 shows results of calculations with different numbers of meshes are presented together with an analytical solution. A relatively simple way to increase the accuracy of the Godunov scheme to the second-order in space and time has been shown by van Leer [16]. Such a second-order shock capturing scheme requires four times less number of meshes than the first-order scheme for the same accuracy.

In these calculations we use a monotonic numerical scheme in which numerical oscillations are not produced. To estimate how many meshes are necessary to make this smoothing negligible, calculations of proton beam impacts on a thick aluminum target were performed with beam parameters typical of KALIF. The energy of protons was taken to be 0.5 MeV, and the power density was increased linearly with a slope of 0.02 TW/cm^2/ns. These results are shown in Fig. 8. It is seen that increasing the accuracy by increasing the number of meshes allows some details of the pressure profile to be resolved. The details of these results will be explained below.
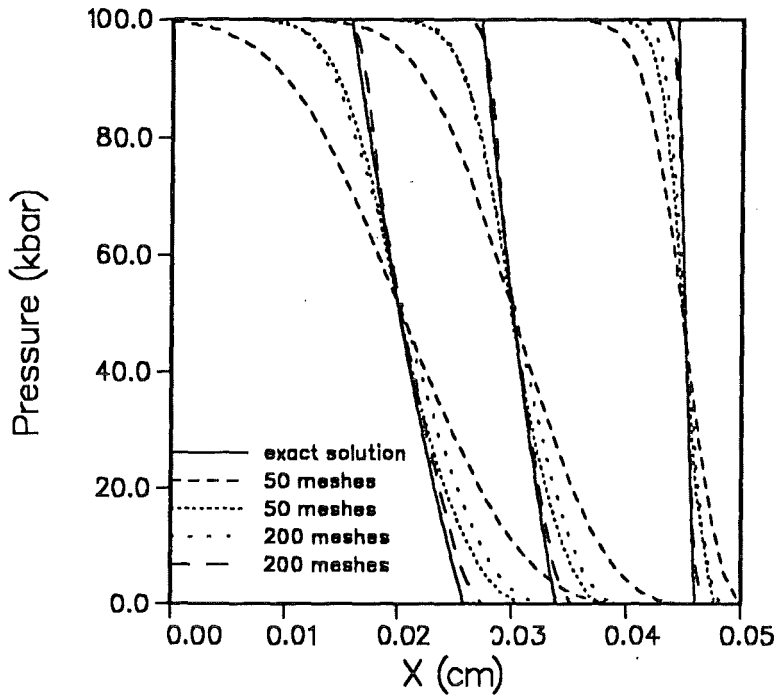
Figure 7. Test calculations: Unloading of an aluminum target. The free boundary is on the right. The exact solution is shown by solid lines, while dashed lines are the results of first and second-order calculations. Times: $t = 10$, $t = 40$, $t = 60\,ns$.
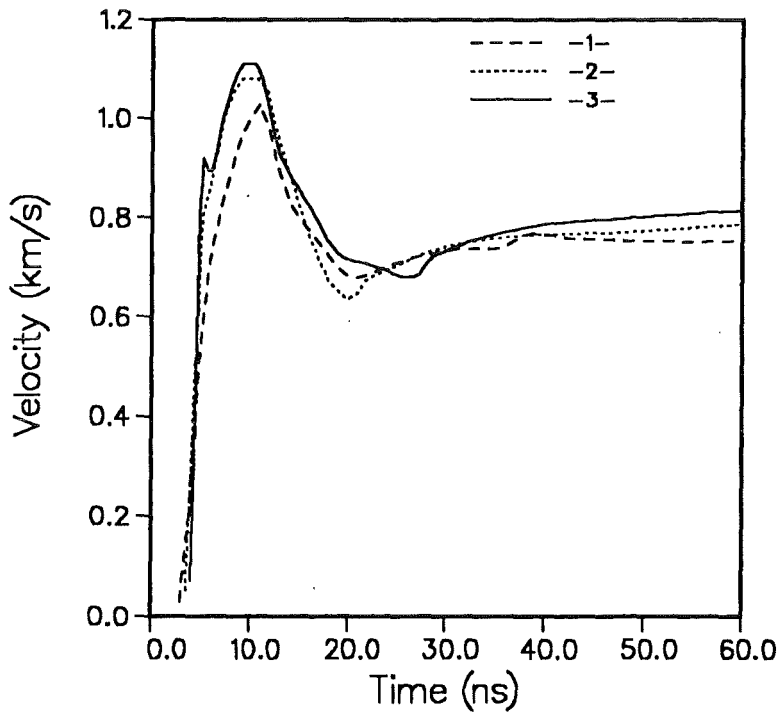
Figure 8. Mass Grid: Mass velocity profiles at a distance of $33\,\mu m$ from the surface. The numbers of meshes used: 1-25, 2-50, 3- 100 meshes with grid refinement.

13

The energy transfer by conductivity is calculated at each time step after hydro-dynamic calculation of the flow parameters, by an implicit finite-difference scheme.

3. Numerical Simulations 3.1 Qualitative Analysis

Real beam power and voltage profiles have a complicated and, often, non-monotonic character. To develop an understanding of the importance of variuos phenomena we start with a qualitative analysis of the pressure generated in the target by an ion beam in a simple situation of constant energy of protons and a constant rise in beam power. The protons energy was chosen to be 0.5 MeV, and the rate of power density rise was taken to be 0.02 TW/cm^2/ns. These values correspond to the initial phase of a KALIF beam. The results of numerical simulations of this case are presented in Fig. 9 to 14. It is seen that the Grüneisen parameter reaches its asymptotic value of 0.4 - 0.5 already in the first few ns. The evolution of the state of matter in the ablation zone, together with phase transition lines for aluminum, is presented in Fig. 12.
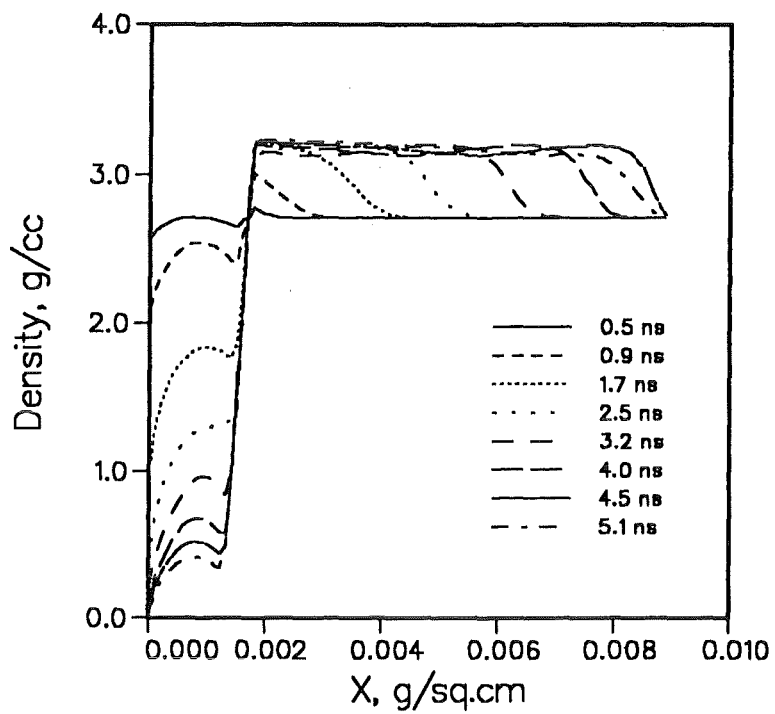
Figure 9.   Density evolution with time.
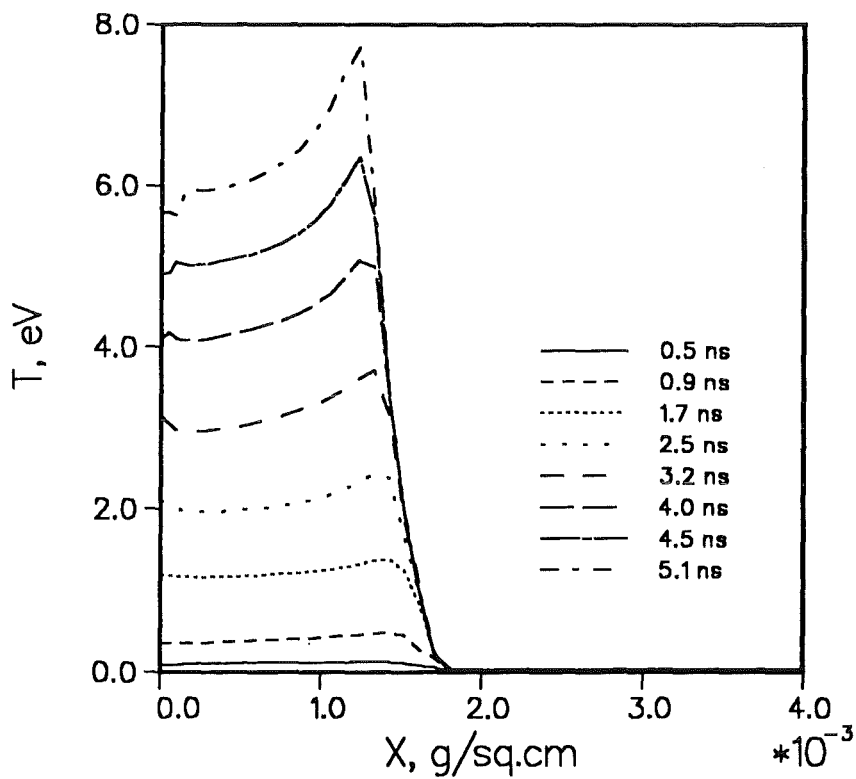
Figure 10.   Temperature evolution with time.
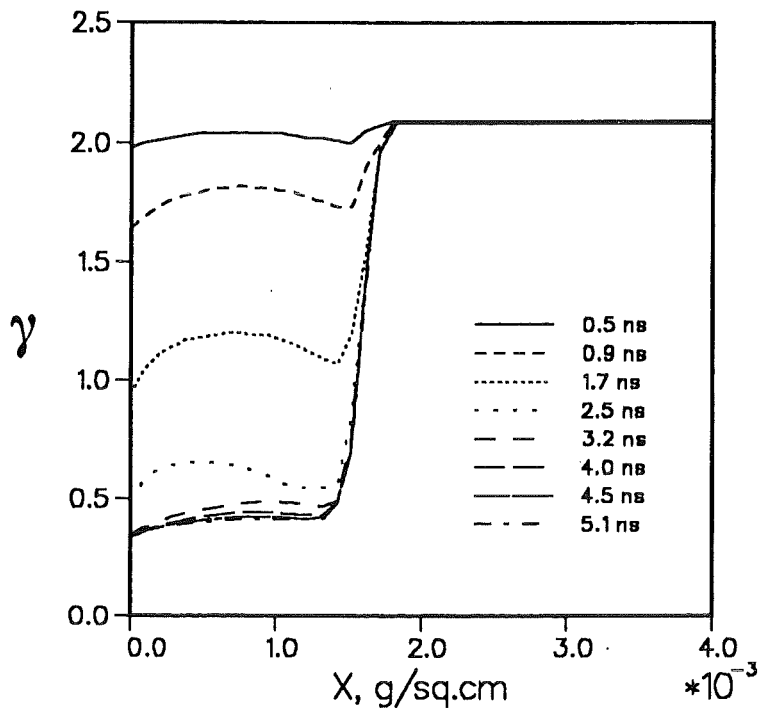
Figure 11. Evolution of the Grüneisen coefficient.
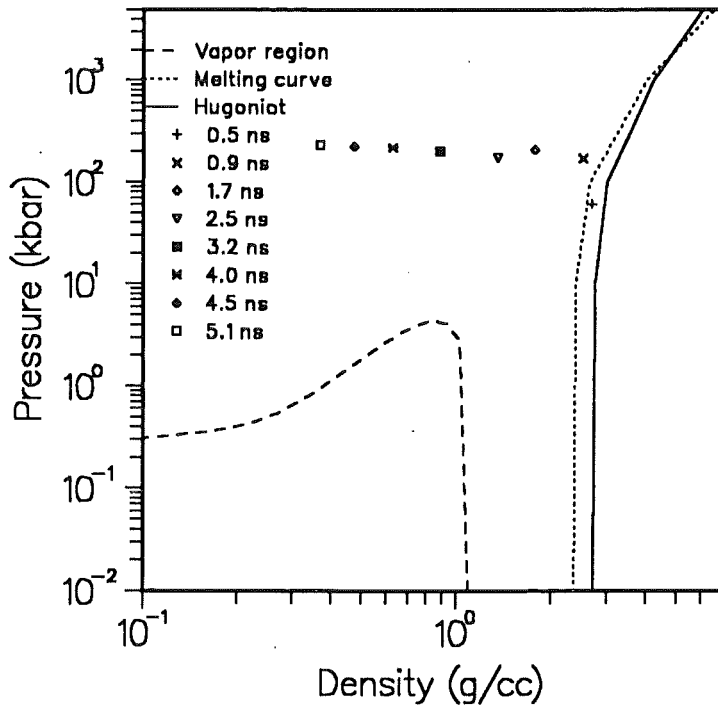
Figure 12. Evolution of the state of matter.

How does the pressure evolve in the energy deposition zone of the target in a case like this? In Fig. 11, it is seen that the Grüneisen parameter, γ, reaches its asymptotic value of approximately 0.4 within the first 3 ns of the beam action. The matter in the energy deposition zone is liquefied within the first ns (Fig. 12). Thus, at a certain level of power growth typical for KALIF, the thermal component of the equation of state prevails over the cold part (which is of the order of 5 kJ/g for aluminum). Thus, for rough estimates, we can disregard the cold part of the EOS. The thermal component of the pressure is a product of the internal specific energy, the Grüneisen parameter and the density. Thus, $P_T = \gamma(E,\rho)E_T\rho$ and the density of deposited beam enregy is $E(t) = P(t).t \sim t^2$. Since the velocity also grows with t, the volume also grows with t^2. Once the Grüneisen parameter has reached its asymptotic value, the pressure in the ablation zone remains constant as long as the power density rises linearly. The behaviour of the pressure during first 4 ns, in which γ drops to its asymptotic value is shown in Fig.12. Constant pressure in the ablation zone means that, if the thickness of the target is finite, the solid part of the target experiences a constant acceleration as long as the power increases linearly. For constant power density, the pressure rises to some maximum value and then starts to decrease due to the expansion of the ablation zone. Fig. 14 shows results of numerical simulations for constant proton energy and constant power. The two curves at the top are for a constant value of γ and show that, the lower the value of γ, larger is the time required to obtain the peak surface velocity. The two lower curves are for EOS1 and EOS2. The Grüneisen parameter reaches some minimum value and then rises slowly. Thus at the start of the beam action the pressure profile is much more complicated than the simple argument above would suggest.
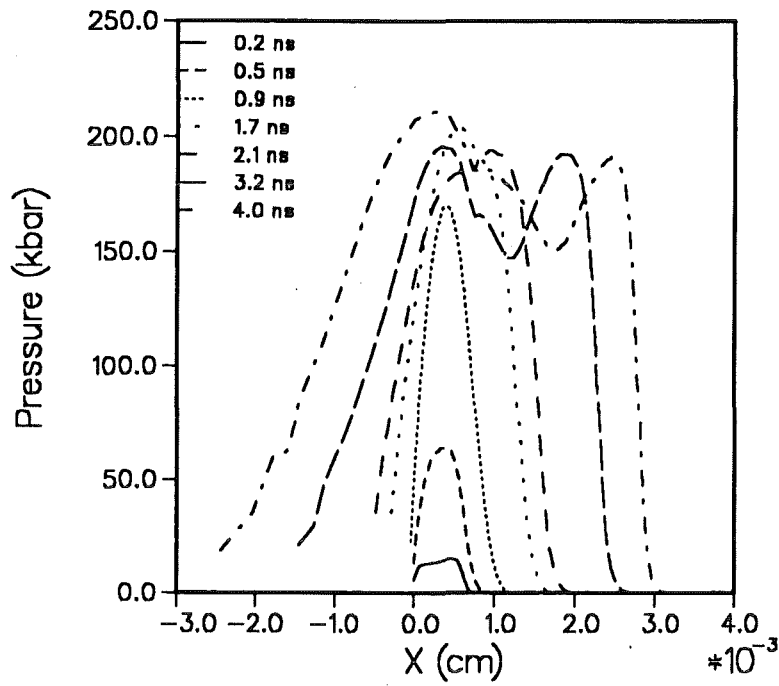
Figure 13. Pressure evolution with time.
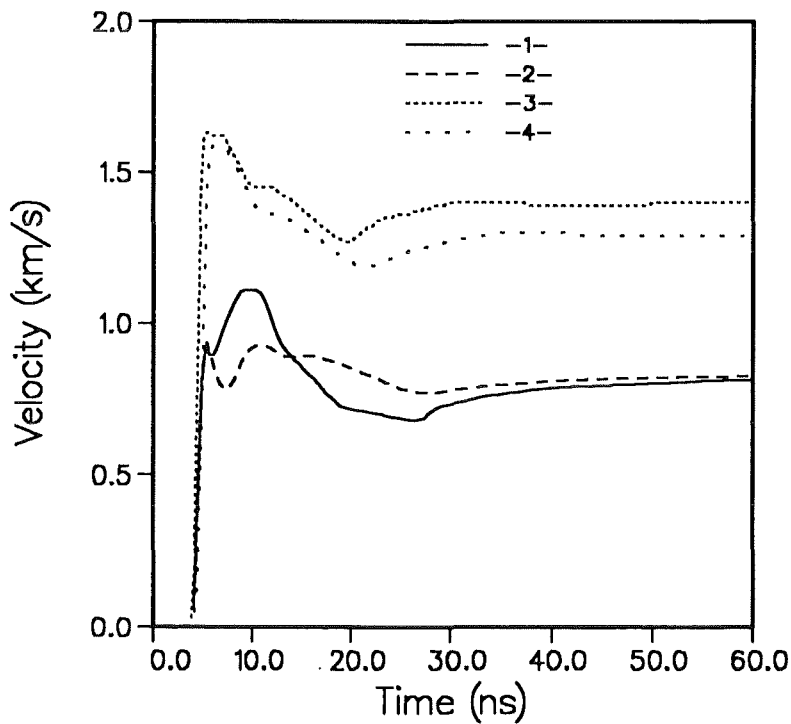
Figure 14. : Mass velocity profiles at a   distance of 33 μm from the surface obtained with various EOS models: 1-EOS2,   2- EOS1, 3- Grüneisen model with $\gamma \equiv 2$. and 4- $\gamma \equiv 1$.

The details of the pressure profile in the first 5 ns depend on the behaviour of the Grüneisen parameter in the condensed, heated matter. The first pressure drop after 1-2 ns can be explained by the decrease of the Grüneisen parameter in the heated matter. In EOS1 γ depends more strongly upon the volume than in EOS2. This is why the use of EOS1 causes a larger drop in surface velocity after the first peak.

Resuming these qualitative analyses one can say that details of the development of Grüneisen parameter with heating and expansion of matter influence the pressure calculation in the energy deposition zone only during the first 5 ns. Afterwards, the pressure is determined by the asymptotical value of the Grüneisen parameter. If the power density grows linearly, we obtain an approximately constant thermal pressure. This means that, if the thickness of the foil is finite, such pressure will accelerate the solid part of the foil at a constant rate. If we use a constant power density, the pressure reaches some peak and then decreases again. In Fig. 15 results of numerical simulations obtained by assuming a constant proton energy of 0.5 MeV and different constant power densities of the beam are presented.

The steps in the velocity profiles correspond to the times at which the waves are reflected at the solid-plasma boundary. The amplitudes of the velocity jumps correspond to the pressure acting on the boundary. It is seen that the jumps in velocity are becoming smaller each time. Thus indicating a decrease of the driving pressure in the energy deposition zone.

5.0

— ω=0.01 TW/sq.cm
- - ω=0.05 TW/sq.cm
···· ω=0.1 TW/sq/cm

4.0

Velocity (km/s)

3.0

2.0

1.0

0.0

0.0   5.0   10.0   15.0   20.0   25.0   30.0

Time (ns)
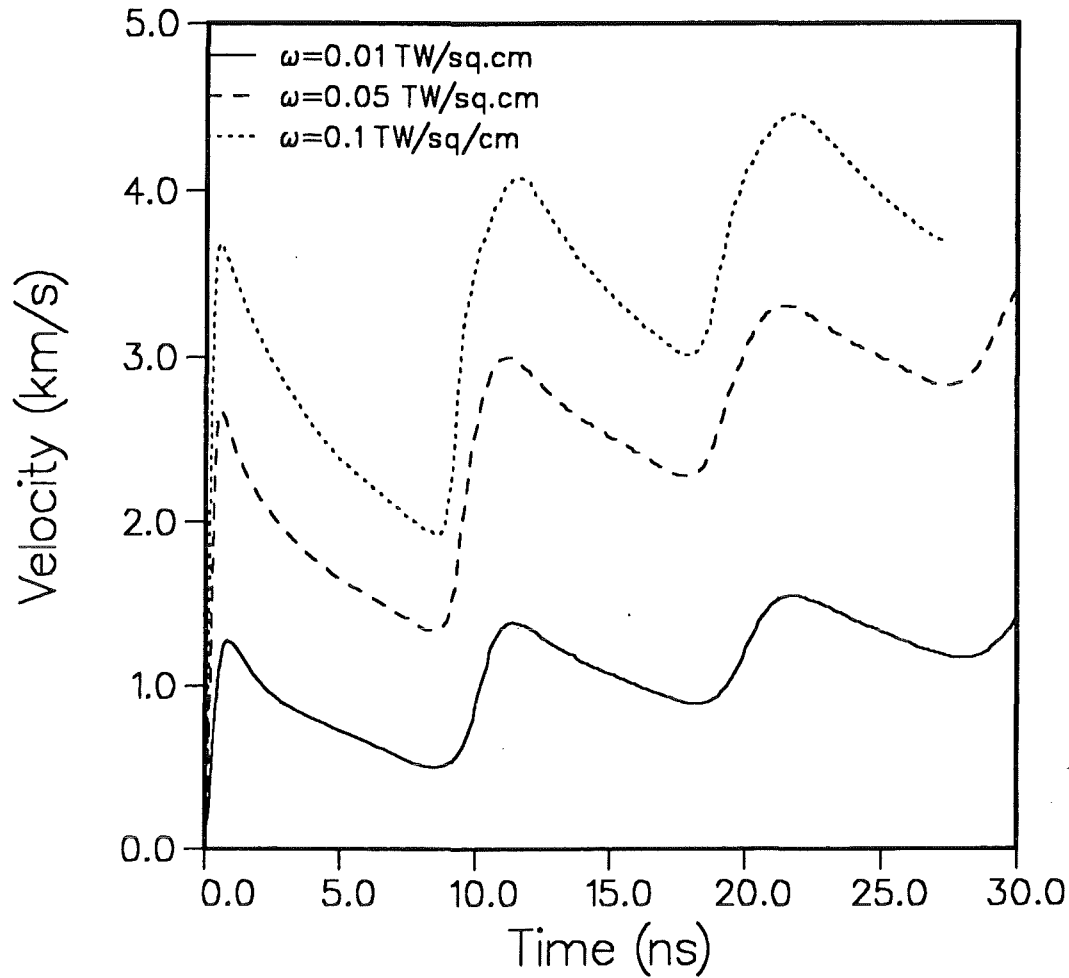
Figure 15. : Free surface velocity of 33 μm aluminum foil as a function of time for different beam power densities.

3.2 Multilayer Targets

This section contains an analysis of the possibility to increase the efficiency of the ion beam by using a cumulating system, such as a multilayered system. The hydrodynamic efficiency, η, ($\eta = E_k/E_0$, with E_k as the payload kinetic energy and E_0 as the absorbed beam energy), of the target can be increased by the multilayered targets. This step has been analyzed analytically [17] with various simplifications, such as the ideal gas equation of state, constant ion energy, and constant beam

power, uniform deposition of the beam energy in the target. These analytical results were verified against realistic models for the equation of state, beam energy deposition as a function of density and temperature, etc. [18]. The basic idea is to use a tamper layer of high-Z material with low stopping power and heavy mass, a low-Z material as absorber in which most of the energy is absorbed and the expansion of the absorber accelerates the pay load. The thicknesses of different zones (tamper - absorber - payload) depend upon the properties of the materials and of the impinging beam. The optimum ratio of the mass of the payload to the total mass was found to be between 0.2 and 0.3 [19], The mass of the absorber and the tamper is determined by the range of the ions. The thickness of the payload, in turn, cannot be below a certain limit, because of manufacturing constraints and because of the possible instabilities have to be avoided. This would suggest the use of a low-mass payload. On the other hand, higher dynamic pressures can be achieved by payloads with large impedance.

The calculations mentioned above were performed for a proton energy of 3 MeV. This energy is about a factor of 2 higher than the energy to which protons currently can be accelerated at KALIF. Let us examine below how the low proton energy influences these results.
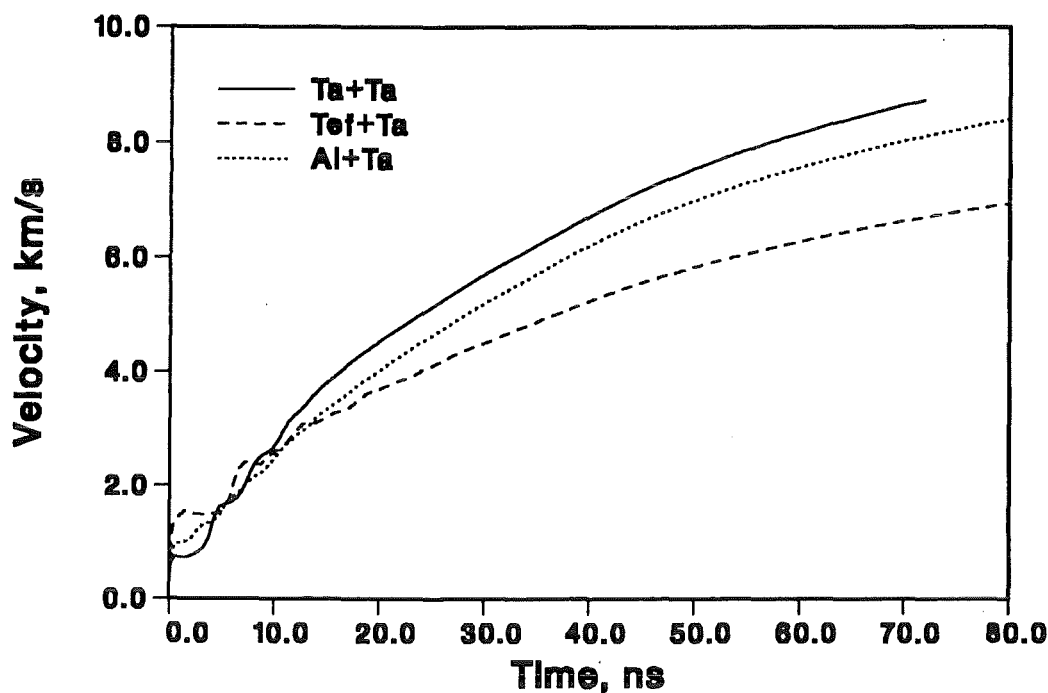
Figure 16. Velocity evolution: Mass velocity of a 5μm Ta payload with different absorbers. The beam used was that of KALIF shot No. 3155. The thicknesses of Teflon or Aluminum absorbers were defined so that the beam was completely stopped in the absorber.

Fig. 16 shows the velocity evolution of a constant payload of 5 μm Ta with various absorber materials. For these calculations, the measured time-dependent beam profile for a KALIF proton beam was used. It is seen that, in the absence of a tamper, the use of a lighter absorber is not recomended, as the center of mass is shifted towards the payload. Placing a tamper layer in front of aluminum improves the results only slightly (Fig. 17). The fixed payload mass and the short range of 1.5 MeV protons prevents the benefits of a layered target from being exploited. The final payload velocity can be increased by reducing the payload mass, i.e. changing from Ta to Cu and keeping the thickness unchanged.
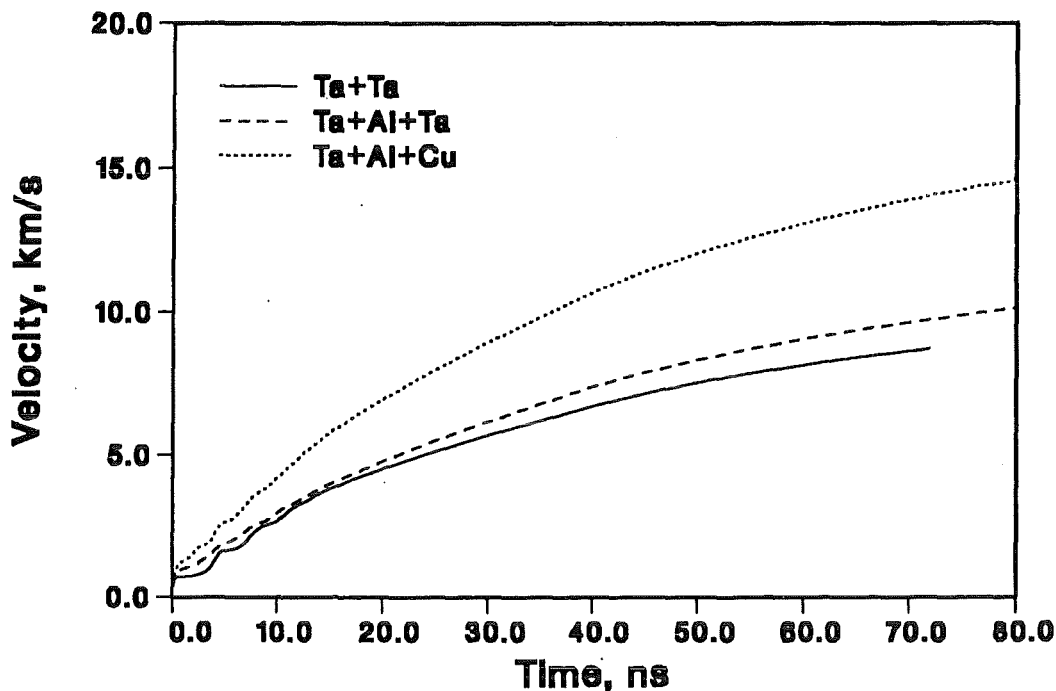
Figure 17. **Velocity evolution:** The mass velocity of a $5\mu m$ payload with different absorbers and a $2\mu m$ Ta tamper. The beam was that of KALIF shot No. 3155. The thickness of a Teflon or Aluminum absorber was set so that the beam was completely stopped in the absorber.

KALIF will be upgraded with the HELIA module in near future. The ion energy in the upgraded KALIF will be about a factor of 4 higher and the power density is expected to be between 1 and 2 TW/cm^2. As the range of 6 MeV protons is about a factor of 10 larger than that of 1.5 MeV proton more flexibilty is availble in the design of a multlayered target. For example the range of 6 MeV protons in solid aluminum is 259 μm, and that of 1.5 MeV protons is 27 μm. In such a case, optimization of the target can lead to an effective cumulative system. The target geometry can be chosen such that the center of mass is located at the tamper absorber interface (see Fig. 18). We have performed calculations for a 10 μm Ta payload acceleration under the beam condition expected in the KALIF-HELIA module. Calculations predict that a pressure of the order of several Mbar can be produced in the absorber of a suitably designed multilayered target for the

23
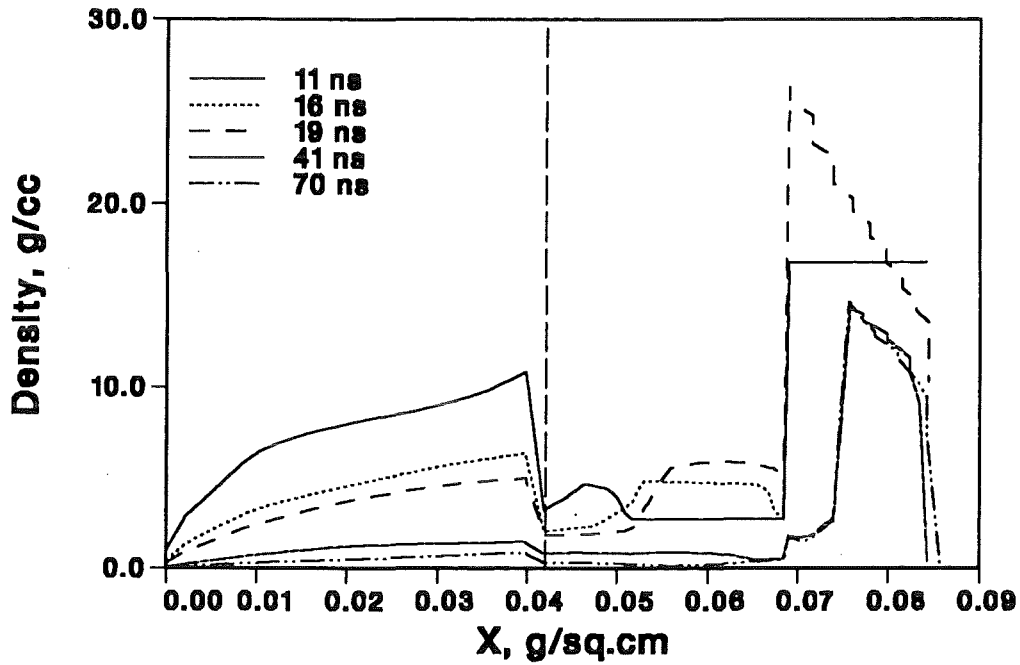
Figure 18. **HELIA:** Density profile for 1 TW/cm^2 and a 6 MeV proton beam. The target dimensions are 25 μmTa, 100 μmAl, and 10 μTa.
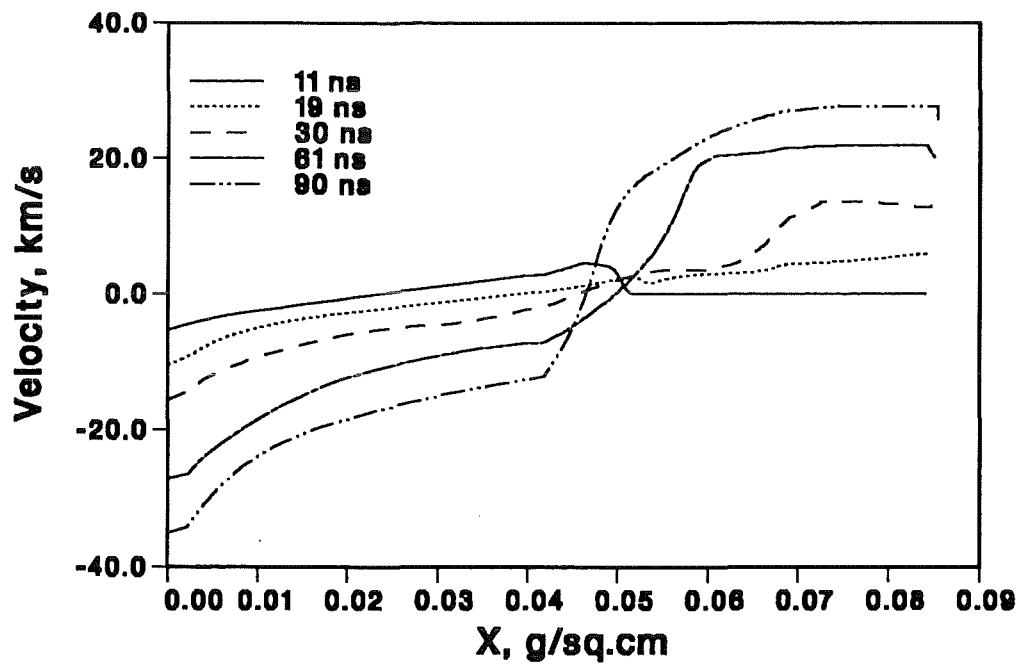
Figure 19. **HELIA.:** Velocity profile for the same target as in Fig. 18.
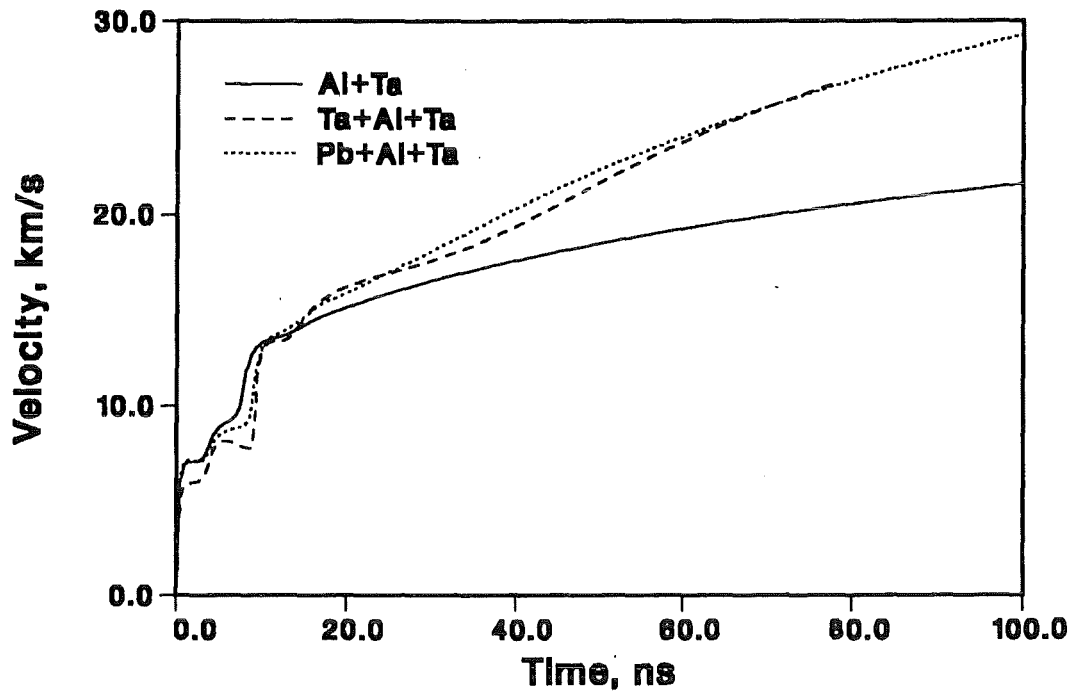
Figure 20. HELIA: Surface velocity evolution for the same conditions as in Fig. 18, but different absorbers.

Due to the greater range, the temperatures in the target are of the same order order of magnitude as in the case of KALIF beam with lower beam power. During the beam puls-action 10 μm Ta payload will be accelerated to 30 km/s in the case of the tampered absorber while for uniform absorber only 20 km/s can be achieved. As one can see from the density profile (Fig. 9) approximately 1/4 of the payload will be vaporized and 3/4 (central part) will melt during the acceleration phase because of the dynamic expansion after the driving pressure decreases.

3.3 Analysis of Experimental Data

At KALIF, foil acceleration and pressure measurements were performed with B_θ and Applied B diodes. The experimental setup is described elsewhere [5]. Three type of experiments were performed: (1) foil acceleration experiments, (2) pressure measurements with an LiF window and (3) experiments with spaced targets.

The results of these three type of experiments of these experiments will be ana-lysed below under the assumption that the beam characteristics did not change in these experiments. In other words, we assume a complete reproducibility of the proton beam in KALIF experiments. This assumption is justified for this analysis, because at present, not all the beam parameters are measured in each shot and as will be shown later the change of the pulse duration and amplitude required to match experimental results is much larger than the expected variation of these parameters between the shots. The electrical signals on the diodes were meas-ured regularly and showed no major differences for successful shots. The total beam intensity was measured to characterize the beam power by nuclear diag-nostics and, because of the experimental constraints cannot be performed to-gether with the foil acceleration experiments analyzed below.

(1) Foil acceleration experiments: In these experiments, thin superrange (i.e. the thickness of the target was larger than the range of protons) aluminum foils of various thicknesses were irradiated by the KALIF beam. The back surface velocity was recorded with ORVIS. The thickness of the targets varied between 22 μm and 75 μm. The very first attempt to simulate the foil acceleration experiments showed that with the experimentally observed beam profile it was not possible to the match the calculated foil velocity results to those of experiments. The simulation results predict velocities much higher than thos observed in experiments. As there is some uncertainty about the beam parameters, we changed the power profile as a function of time to obtain a reasonably good agreement between the calculated and the measured foil velocities. This comparison is shown in Fig.21. For this agreement to be reached we had to reduce both the height and the du-

ration power profile as a function of time. The fitted power profile is marked Number 1.

If the experimental observation of the diode voltage and current is used to derive beam profile as a function of time it will lead to the profile similar to profile Number 3, with a peak power density of the order of 0.2 TW/sq.cm. The ion energy of the beam particles was derived from the diode voltage and was not varied in these calculations.
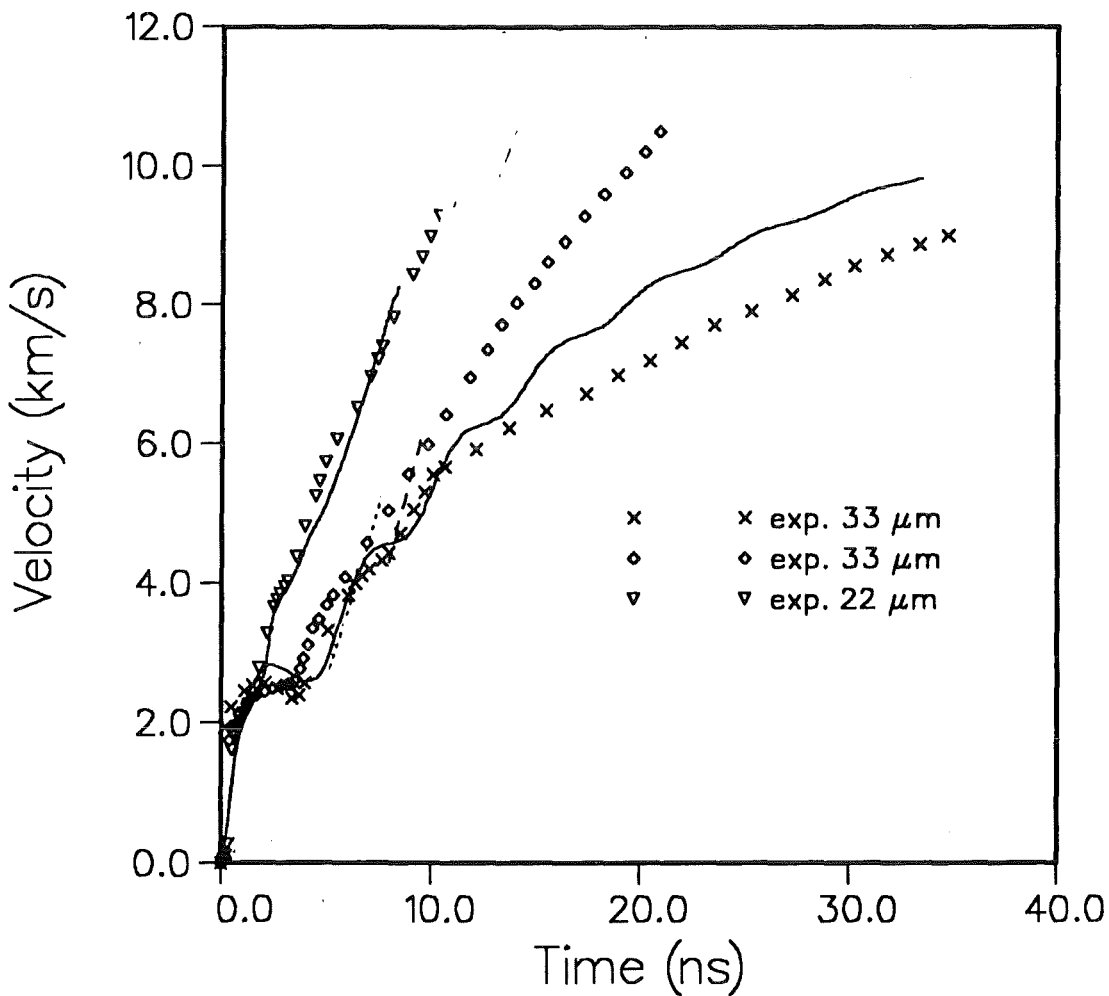
Figure 21. : Experimental data and results of simulations for 22 μm and 33 μm aluminum foils.
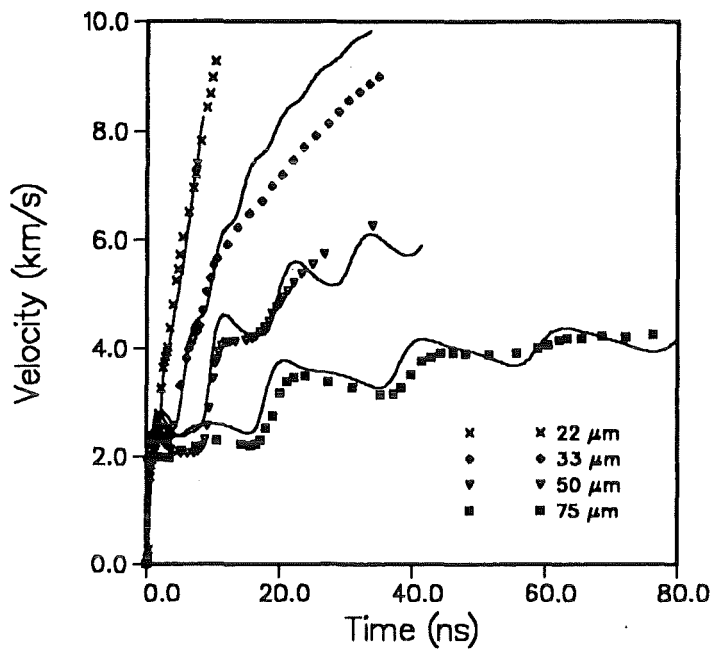
Figure 22. : Experimental data and results of simulations for *22 μm*, *33 μm*, *50 μm*, and *75 μm* aluminum foils.
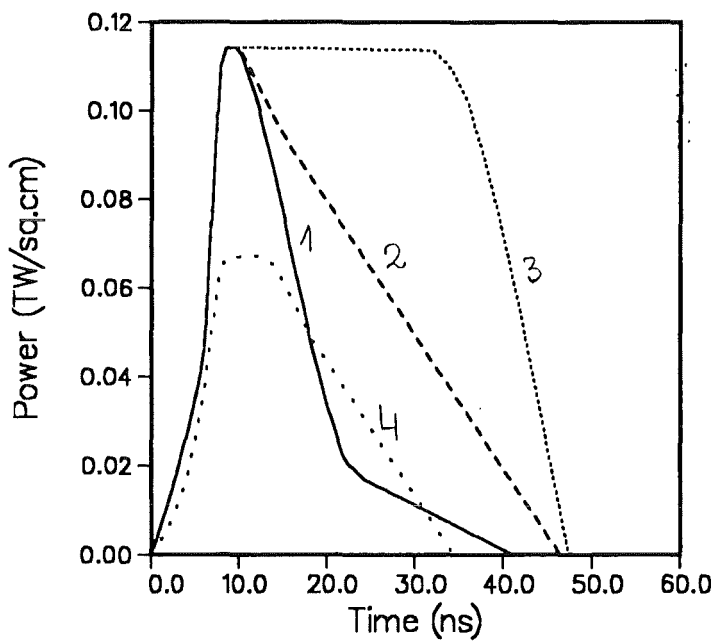
Figure 23. : Power density profiles used in calculations. The total energy densities are 1- 1.5 kJ/cm², 2-2.5 kJ/cm² , 3- 4.1 kJ/cm² , 4-1.2 kJ/cm² .

28
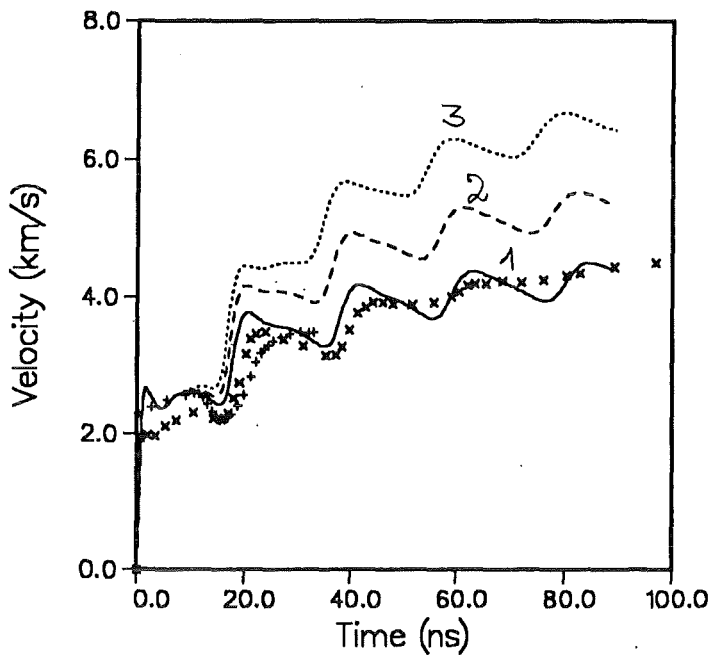
Figure 24. : Experimental data and results of simulations for 75 μm aluminum foils with various power profiles.

2) Pressure measurements: In these experiments the aluminum foils, whose thicknesses slightly exceeded the range of protons, were covered with LiF windows to avoid shock reflections. The impedance of LiF is approximately the same as that of aluminum. The velocity at the Al-LiF interface was recorded as a pressure signal. The LiF window experiments should furnishes more direct information on pressure. The results of two such experiments are plotted in Fig. 22. The experimental data (symbols) indicate that the pressure in the energy deposition zone drops after about 10 ns. This behaviour is also reproduced by profile Number 1. However, this profile causes a larger decrease in the Al-LiF interface velocity than was observed in experiments. The profile Number 2 reproduces the experimental results fairly well. This profile is slightly broader than the profile Number 1, but much narrower than profile Number 3.
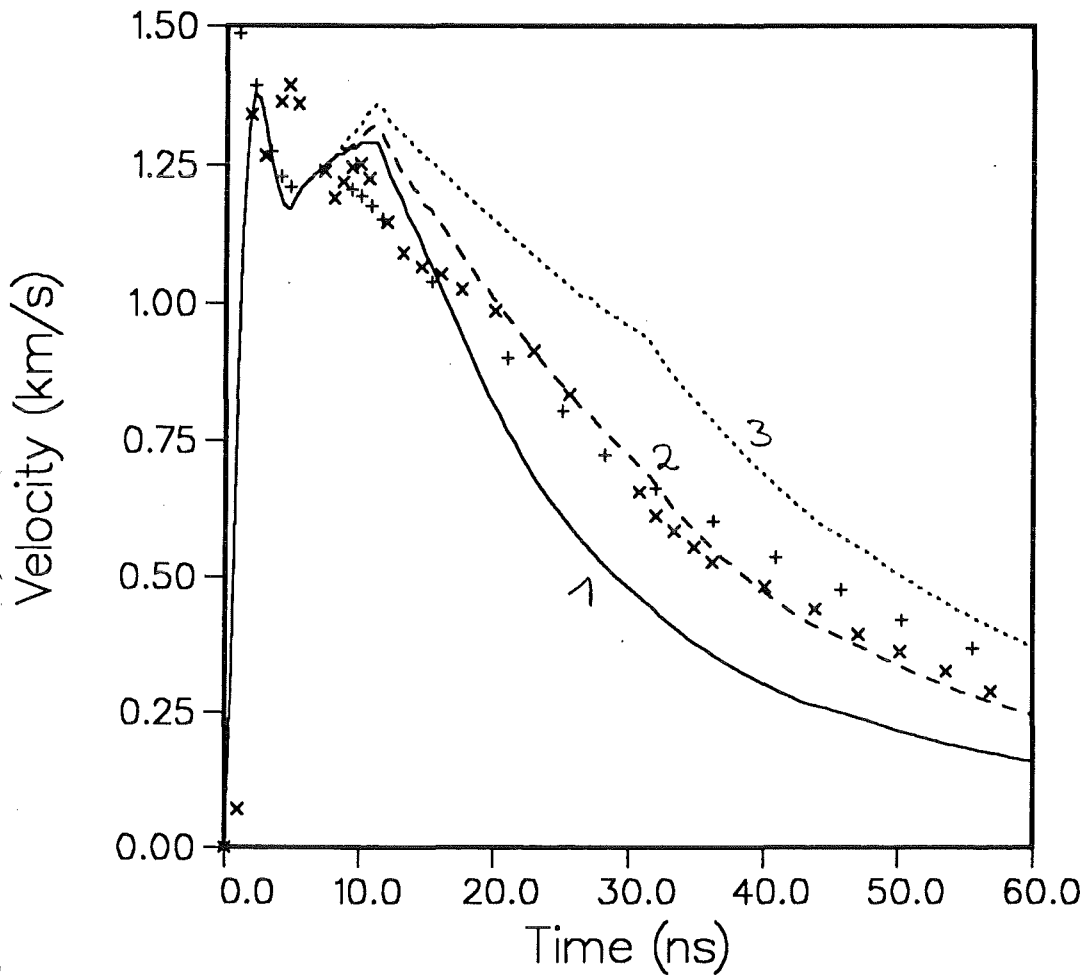
Figure 25. : Experimental data and results of simulations for a 33 μm aluminum foil with LiF windows. Lines correspond to calculations with the same voltage profile and different power profiles shown in Fig. 23.

3) Spaced targets: In these experiments, two thin aluminum foils were placed at a distance from each other. The distance between the foils was chosen sufficiently large (2 mm) so that the plasma generated from the first foil did not reach the second foil during measurement. The thickness of the first target was less than the range of maximum-energy protons. Protons reaching the second target were reduced in their energy by the first target.
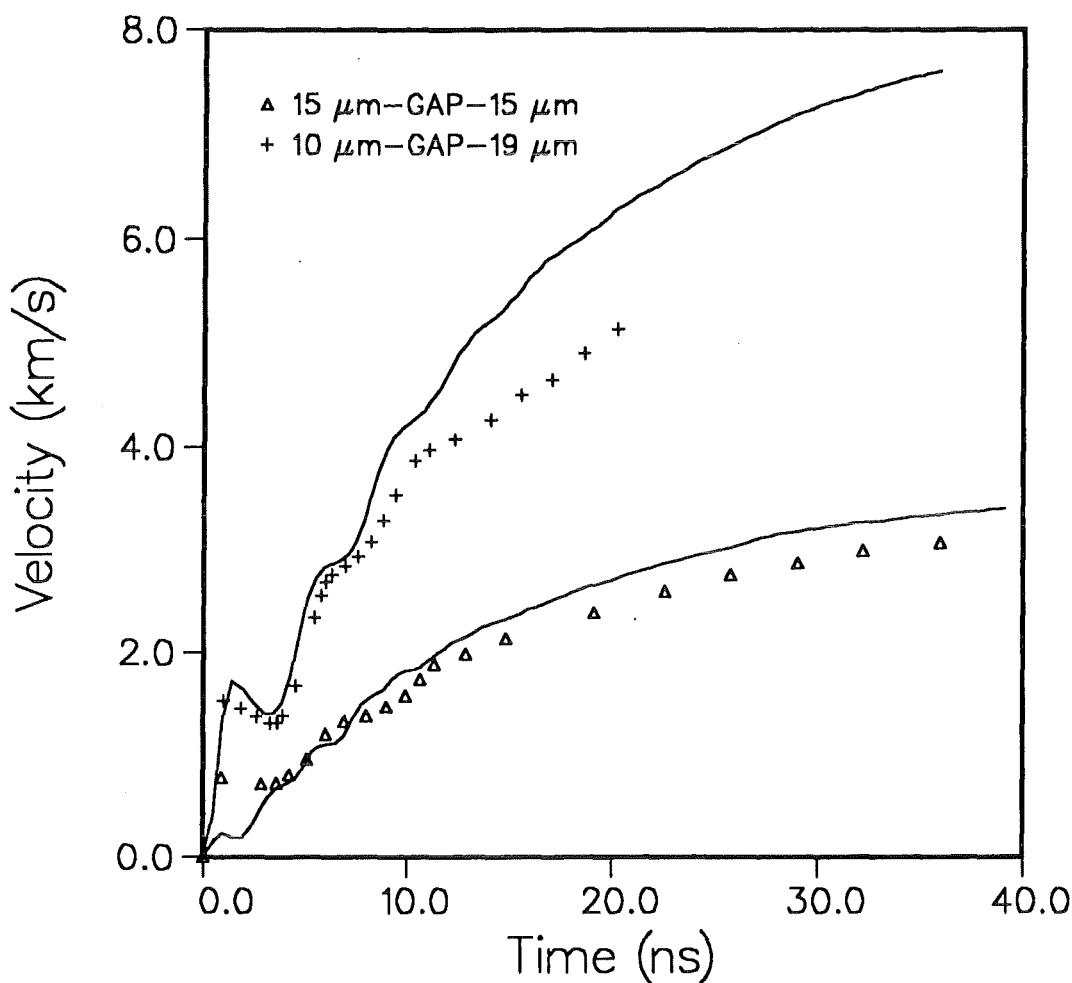
Figure 26. : Experimental data (points) and results of simulations (lines) for spaced aluminum targets.

Using power profile Number 1 we also simulated this type of experiments. Results of these calculations are presented in Fig. 26. For better agreement with the experimental results, in this case, not only the power profile but also the voltage (i.e. proton energy) evolution as a function of time must be known precisely because the part of the beam power penetrating through the first foil is determined mainly by the energy of the protons. It should mention at this poit that the energy of protons of approximately 1-1.4 MeV drops to 0.1-0.3 MeV after penetration through the first foil. The stopping power at such low proton energies show con-

siderable uncertainty. Fig. 6 showed the range of protons at typical temperatures and densities calculated with the present model to be considerably different from that calculated with the model used previously [13]. This comparison therefore is of little interest at present. However, if the beam parameters are known exactly, such experiments can be used to verify the stopping power models used.

3.4 Effects of the Equation of State
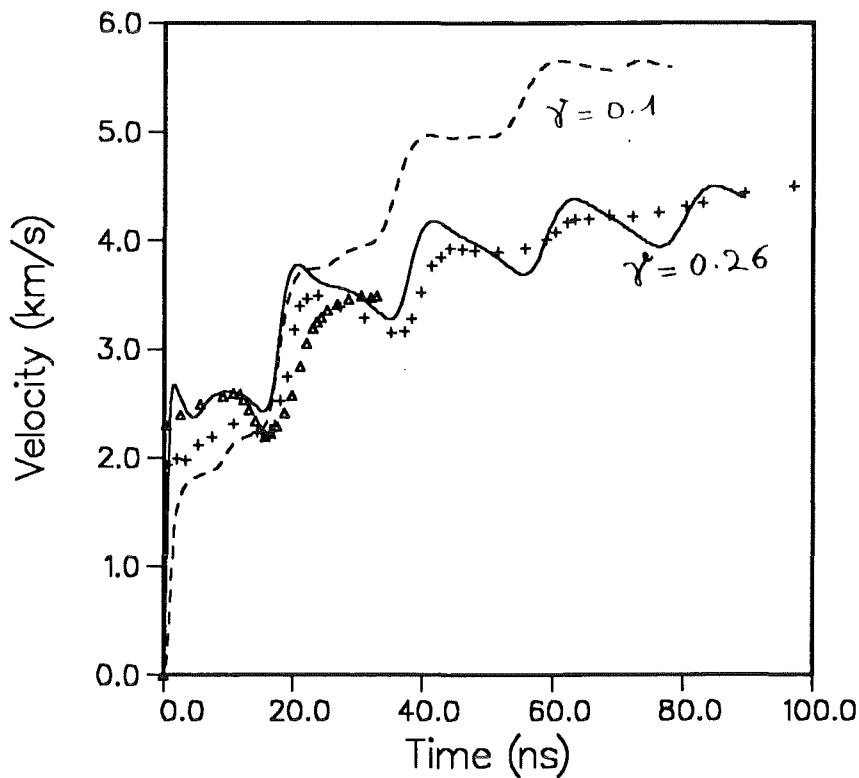
Figure 27. : Experimental data and results of simulations for 75 μm foils obtained with various values of γ_a

To be sure that the difference in the temporal beam power profile between the experiment and the calculations is not due to an inadequate equation of state we repeated these calculations with changed equation of states. The main parameter

in the equation of state is the asymptotic value, γ, and its variation with temperature and density. The effect of the variation of γ is important only in the initial phase of the beam action. The asymptotic value of γ is is reached within the first 5 ns. Fig. 27 shows the results obtained with the two different dependences of γ for 75 μm aluminum. Again, beam profile Number 1 with the functional dependence of γ of Eq. 2.14 reproduces the experimental data better than that of Eq. 2.15. With a change in the temporal beam profile, EOS2 can also lead to better agreement between the experiment and the calculations but, in this case, the peak beam power has to be reduced even more than is required in profile Number 1. Changing the asymptotic value of γ also does not lead to a better agreement even if γ is reduced to an unrealistically small value.
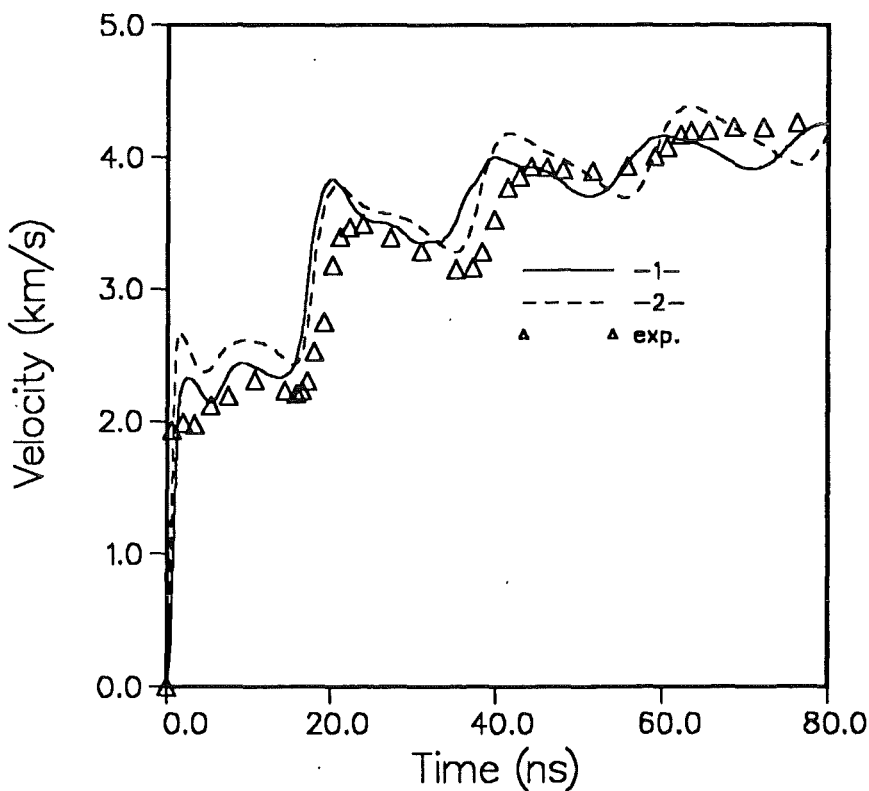
Figure 28. : Experimental data and results of simulations for 75 μm foils obtained with the two functions for $\gamma(E,V)$; 1- EOS2, 2- EOS1.

5. Summary and Conclusions

Foil acceleration experiments performed at KALIF, in which thin foils were accelerated to 12.5 km/s were analysed. In our calculations we assumed the equation of state to be composed of two parts. The first part describes the cold curve, the second part describes the thermal component of the equation of state. In KALIF-type experiments, the thermal component of the equation of state is of prime importance. We studied this part in more detail. We assumed, for this purpose, that the Grüneisen parameter is a function of density and temperature. Its asymptotic value was taken from the ralevant theoretical models. The advantage of this treatment is that the uncertainty in the equation of state data is reduced to the uncertainty in the value of γ. In this way we studied the evolution of γ in the target plasma. For the transition of one asymptotic limit to the other two different functions were used. We studied the evolution of γ in the target plasma. The transition of γ from the solid state value to the asymptotic plasma value (0.4) occurs in the first few ns. Thus, if the beam parameters are known exactly, the function $\gamma(T, \rho)$ can be fixed by accurate measurement of the Al-LiF interface velocity for the first 10 ns.

Our results indicate that the beam power profile as a function of time differs appreciably from that derived from the electrical signals at the diode. The difference is in the peak power as well as in pulse duration. For both these quantities, our results are about a factor 2 lower. We checked our numerical method for possible reasons for this discrepancy. The discrepancy cannot be explained by the uncertainty in the equation of state data.

6. Acknowledgment This work was partly done wihin the Science and Technology Cooperation program between Germany and Russia.

7. References

[1]   K. Baumung et al., Hydrodynamic Target Experiments with Proton Beams at KALIF, Proc. Ninth International Conference on High-Power Particle Beams, (ed. D.Mosher, G.Cooperstein), May 25-30,1992, Washington DC, USA , Vol. I. p.68.

[2]   B. Goel, O.Yu. Vorobjev, A.L. Ni, Generation of Ultra High Pressure with Light Ion Beams, Proc. Ninth International conference on High-Power Particle Beams, (ed. D.Mosher, G.Cooperstein), May 25-30,1992, Washington DC, USA , Vol. II. p.957.

[3]   H. Bluhm et al., Focusing Properties of a Strongly Insulated of a Applied B Proton Diode with a Preformed Anode Plasma, Proc. Ninth International Conference on High-Power Particle Beams, (ed. D.Mosher, G.Cooperstein), May 25-30,1992, Washington DC, USA , Vol. I. p.51.

[4]   T.A. Mehlhorn et al., Progress in Lithium Beam Focusing and Beam-Target Experiments at SANDIA, Proc. Ninth International Conference on High-Power Particle Beams, (ed. D.Mosher, G.Cooperstein), May 25-30,1992, Washington DC, USA , Vol. I. p.31.

[5]   K. Baumung et al., Light-ion Beam-Target Interaction Experiments on KALIF, Nuovo Cimento 106 A (1993) 1771

[6]   A.V. Bushman, G.I. Kanel, A.L. Ni, V.E. Fortov, Thermal Physics and dynamics of Intense Pulse Action, Inst. of Chemical Physics, Chernogolovca (1988).

[7]   Ya.B. Zeldovich, Yu.P. Raizer, Physics of Shock Waves, Academic Press, 1967.

[8]   Lawrence Livermore National Laboratory, Report UCID-118574-82-2 (1982).

[9]   G.D. Tsakiris, K. Eidman, JQSRT 38 (1987) 353.

[10] A.V. Bushman, V.E. Fortov, I.V. Lomonosov, Proc. Enrico Fermi School 1989, Elsevier Publ. 1989 p. 249

[11] A.F. Nikiforov, V.G. Novikov, S.K. Truxanov, V. Uvarov, Preprint No. 137, 1989, Moscow.

[12] A.Ya. Polyshchuk, V.E. Fortov, V.S. Khloponin, Sov. J. Plasma Phys. 17 (1991) 523.

[13] B. Goel, H. Bluhm, Determination of Proton Stopping Power in Hot Plasma at KALIF, J. de Physique, C7-49(1988)C7-169.

[14] W. Ebeling, A. Föster, V.E. Fortov, V.K. Gryaznov, A.Ya. Polishchuk, Thermophysical Properties of Hot Dense Plasmas, Teubner-Texte zur Physik, Bd. 25, Teubner Verlag, Stuttgart-Leipzig 1991

[15] S.K. Godunov, Finite Difference Method for Numerical Computation of Discontinuous Solution of Equations of Fluid Dynamics, Mat. Sbornik 47 (1959) 271.

[16] B. van Leer, Towards the Ultimate Conservative Difference Scheme. V., A Second Order Sequel to Godunov's Method, J. Comput. Phys. 32 (1978) 101.

[17] A. Ng, A.R. Piriz, Phys. Rev.A 40 (1989) 114.

[18] O.Yu. Vorobjev, A.L. Ni, V.E. Fortov, Sov. Tech. Phys.Lett. 16 (1990) 11.

[19] A.R. Piriz, Plasma Phys. & Contr. Fusion, Vol. 30, (1988) 793.